GPH-International Journal of Applied Science
(Online ISSN 3050-9653)
Volume 09 | Issue 05 | 2026
Published by: Global Publication House
DOI: https://doi.org/10.5281/zenodo.21396565
Available online at: www.gphjournal.org
Journal homepage: https://gphjournal.org/index.php/as/index

Semi-Analytical Study of Transient Magnetohydrodynamic (MHD) Axial Flow in a Permeable Annulus

Jibrin Danjuma Yahaya[1], Raji Muhammed[1], Agbata Benedict Celestine[1], Adaji Isaac[1], Ibrahim Aminu[1], Abraham Ayegba Alfa[2], Jacob Funsho Omonile[3]
[1]*Department of Mathematics and Statistics, Confluence University of Science and Technology, Osara, Kogi State, Nigeria*
[2]*Department of Computer Science, Confluence University of Science and Technology, Osara, Kogi State, Nigeria*
[3]*Department of Physics, Confluence University of Science and Technology, Osara, Kogi State, Nigeria*
Corresponding Author: Jibrin Danjuma Yahaya; E-mail: yahayajd@custech.edu.ng

Abstract

This study investigates transient magnetohydrodynamic axial flow of an incompressible, viscous, electrically conducting Newtonian fluid through a porous annulus bounded by two stationary concentric cylinders. The flow is driven by a constant axial pressure gradient and subjected to a uniform transverse magnetic field. Darcy resistance is used to represent porous-medium drag, while the Lorentz-force term accounts for magnetic damping under the low-magnetic-Reynolds-number approximation. The governing momentum equation is non-dimensionalized and solved using the Laplace transform method, with numerical inversion performed by the Riemann-sum approximation. Steady-state expressions for velocity and wall shear stress are also obtained for comparison with the large-time behaviour of the transient solution. The results show that magnetic and porous resistances combine through $\alpha^2 = M^2 + 1/Da$. Increasing the Hartmann number reduces the axial velocity, while increasing the Darcy number enhances the flow by reducing porous resistance. The transient velocity and skin friction approach their steady-state limits as time increases. The formulation may be useful for idealized studies of hydromagnetic transport in porous annular systems.

Keywords:

Magnetohydrodynamics; porous annulus; transient axial flow; Darcy number; Hartmann number; Laplace transform; Riemann-sum approximation; skin friction; annular flow.

Nomenclature

Symbols	Name/Unit(s)	Dimension
r:	Radial coordinate (m)	(L)
z:	Axial coordinate (m)	(L)
t:	Dimensional time (s)	(T)
R_1:	Radius of the inner cylinder (m)	(L)

R_2:	Radius of the outer cylinder (m)	(L)
$w(r,t)$:	Dimensional axial velocity (m/s)	LT^{-1}
η:	Dimensionless Radial coordinate	
T:	Dimensionless time	
$u(\eta,T)$:	Dimensionless axial velocity	
$u_s(\eta)$:	Dimensionless steady-state axial velocity	
p:	Fluid pressure	$ML^{-1}T^{-2}$
G:	Constant axial pressure gradient	$ML^{-2}T^{-2}$
ρ:	Fluid density	ML^{-3}
μ:	Dynamic viscosity	$ML^{-1}T^{-1}$
ν:	Kinematic viscosity	L^2T^{-1}
σ:	Electrical conductivity of the fluid	$M^{-1}L^{-3}T^3I^2$
B_0:	Applied magnetic field strength	$MT^{-2}I^{-1}$
K:	Permeability of the porous medium	L^2
λ:	Dimensionless radius ratio	$\left(\lambda = \frac{R_1}{R_2}\right)$
M:	Hartmann number	
Da:	Darcy number	
s:	Laplace transform parameter	
$\bar{u}(\eta,s)$:	Laplace transform of the dimensionless velocity	
$I_0(.)$:	Modified Bessel function of the first kind of order zero	
$K_0(.)$:	Modified Bessel function of the second kind of order zero	
$I_1(.)$:	Modified Bessel function of the first kind of order one	
$K_1(.)$:	Modified Bessel function of the second kind of order one	

1 Introduction

Transport phenomena in annular passages are important in theoretical and applied fluid dynamics because annular configurations occur in many internal-flow systems, including heat exchangers, drilling operations, journal-bearing lubrication, filtration devices, and electromagnetic flow-control arrangements. In such systems, cylindrical geometry produces radial variation in momentum diffusion, while the no-slip constraints at the inner and outer boundaries generate wall-shear effects. The complexity increases when the annular region is saturated with a porous medium and the working fluid is electrically conducting, since the motion is then influenced by viscous diffusion, porous resistance, pressure forcing, and magnetic damping. In such systems, the flow geometry produces curvature-induced radial variation in momentum diffusion, while the no-slip constraints imposed at the inner and outer cylindrical boundaries generate strong wall-shear effects. The complexity increases considerably when the annular region is saturated with a porous medium and the working fluid is electrically conducting. In that case, the fluid motion is simultaneously influenced by viscous diffusion, porous resistance, pressure forcing, and magnetic damping.

Unsteady annular and curved-channel flows have been widely studied because the transient development of the velocity field controls the startup shear stress, flow-rate response, and long-time stability of the system. Early and modern studies of Dean-type, Taylor-Couette, and annular flow configurations have demonstrated that curvature, wall motion, oscillation, and axial pressure forcing can significantly modify the structure of the velocity field. Transient Dean flow in annular geometries has been examined using semi-analytical approaches, with an emphasis on the formation of secondary flow effects and the time evolution of the flow field [1], [2]. Generalized Taylor-Couette and Dean-flow configurations have also been investigated to understand the interaction between annular geometry, cylinder motion, and transient momentum diffusion [3], [4]. The stability and velocity-field characteristics of axial flow in annuli with rotating boundaries were studied in classical Taylor-Couette-type configurations [5], [6], while exact and limiting solutions for oscillatory pipe and annular flows have provided useful analytical benchmarks for transient cylindrical transport problems [7].

Recent investigations have extended annular-flow analysis to more sophisticated configurations involving oscillating cylinders, dynamic and static slip, variable viscosity, and dusty-fluid effects. For example, unsteady Dean flow of dusty fluids between oscillating cylinders has been considered in relation to particle-laden cylindrical flows [8], while the influence of variable viscosity on unsteady Couette flow has been shown to introduce important changes in the transient diffusion of momentum [9]. Dynamic and static slip effects have also been incorporated into unsteady magnetohydrodynamic Dean flow models, showing that boundary slip can strongly alter flow resistance and near-wall shear behavior [10]. These studies emphasize the continuing relevance of semi-analytical methods for transient cylindrical and annular flows, especially when exact closed-form time-domain solutions are difficult to obtain.

The presence of porous media introduces additional resistance to the fluid motion. The theory of flow through porous materials is commonly based on Darcy-type drag formulations, where the permeability of the medium governs the degree of resistance encountered by the fluid [11]. Annular and channel flows involving porous walls or porous fillings have been investigated in several contexts. Laminar flow in an annulus with porous walls was studied as an early model of wall transpiration and porous-boundary effects [12]. Transient pressure-driven flow in annuli partially filled with porous material has been examined under azimuthal pressure forcing [13], while Taylor-Dean flow in composite annuli partially filled with porous media has revealed important momentum-exchange effects across clear-fluid and porous-fluid regions [14]. Related studies on composite channels and porous Couette flow have demonstrated that porous resistance can strongly delay the establishment of steady motion and reduce the magnitude of the velocity field [15], [16]. In curved porous channels, permeability and curvature jointly influence the structure of the velocity distribution and pressure-driven transport [17]. These studies establish that porous-medium resistance is a dominant physical mechanism in confined internal flows.

Magnetohydrodynamic flow is another important extension of annular and channel-flow theory. When an electrically conducting fluid moves through a magnetic field, electric currents are induced within the fluid. The interaction between these currents and the imposed magnetic field generates a Lorentz force that generally opposes the fluid motion. This produces magnetic damping, which is useful in flow control, metallurgical processing, electromagnetic pumping, plasma confinement, cooling of nuclear reactors, and liquid-metal transport systems. In annular systems, the magnetic field may interact with curvature and wall constraints to produce strong modifications in velocity and shear stress. The effect of an axial magnetic field on Taylor-Couette flow has been studied with emphasis on hydromagnetic stability and rotational-flow modification [18]. Unsteady Dean flow between concentric circular cylinders in the presence of a magnetic field has also been examined, showing that magnetic-field strength can significantly suppress transient motion [19]. In related channel and annular systems, transient MHD Couette and Poiseuille flows have shown that the Hartmann number acts as a controlling damping parameter [20], [21], [22], [23].

Although many studies have examined transient annular flows, porous-medium flows, and magnetohydrodynamic flows, fewer works have treated the combined influence of Darcy resistance and magnetic damping in a pressure-driven porous annulus using a compact semi-analytical formulation. The present study addresses this problem by considering transient axial flow of an electrically conducting fluid through a porous annular region under a transverse magnetic field. The formulation captures the competition among pressure forcing, viscous diffusion, Lorentz-force resistance, and Darcy drag within a single dimensionless model.

The present work, therefore, develops a semi-analytical model for transient MHD axial flow through a porous annulus bounded by two stationary concentric cylinders. The governing equation is formulated from the axial momentum balance under the assumptions of incompressibility, full development, Newtonian behaviour, negligible induced magnetic field, and Darcy resistance. The model is non-dimensionalised to identify the controlling parameters: the Hartmann number, Darcy number, and radius ratio. The Laplace transform method is then used to obtain the transformed velocity distribution, while the Riemann-sum approximation is used to invert the solution numerically. Closed-form steady-state velocity and skin-friction expressions are also derived to validate the transient solution at large time.

2 Mathematical Analysis and Physical Interpretation

Consider the unsteady, fully developed, pressure-driven axial flow of an incompressible viscous electrically conducting fluid through the annular region between two fixed concentric cylinders. Let the inner cylinder have radius R_1, and the outer cylinder have radius R_2, where $0 < R_1 < R_2$. The fluid occupies the annular region $R_1 \leq r \leq R_2$. The flow is assumed to be axisymmetric and fully developed in the axial direction. Therefore, the velocity field is $\mathbf{V} = (0,0,w(r,t))$, where $w(r,t)$ is the axial velocity, $r$is the radial coordinate, and $t$is time. The cylinders are stationary, so the no-slip condition is imposed on both walls. A constant pressure gradient drives the flow along the axial direction, while a uniform magnetic field of strength B_0 is applied transversely to the motion. The magnetic Reynolds number is assumed to be small, so the induced magnetic field is neglected. The annular region is saturated with a homogeneous and isotropic porous medium of permeability K. The resistance of the porous matrix is described using Darcy's law.

Physically, the axial pressure gradient acts as the driving force. Viscosity diffuses momentum from the annulus interior toward the walls. The magnetic field produces a Lorentz force that opposes the motion of the conducting fluid. The porous matrix also produces a drag force proportional to the velocity. Thus, the transient velocity field is determined by the balance among pressure forcing, viscous diffusion, magnetic damping, and porous resistance. The geometry of the flow physics is given in Figure 1 below:

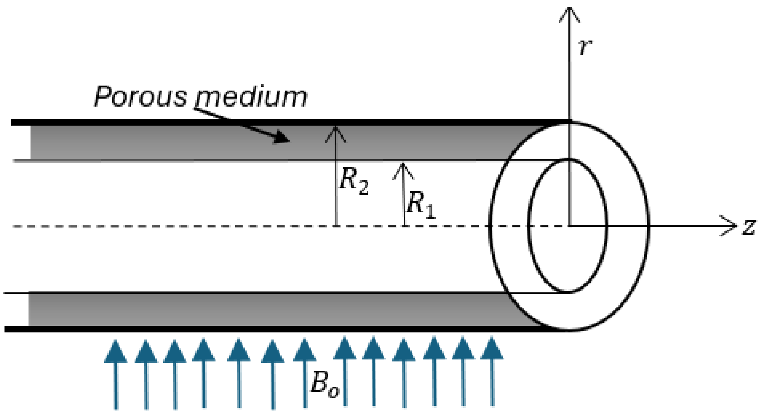

Figure 1: Geometry of the flow physics

2.1 Dimensional governing equations

For the assumed unidirectional axial flow, the continuity equation is automatically satisfied. The axial momentum equation in cylindrical coordinates is:

$$\rho \frac{\partial w}{\partial t} = -\frac{\partial p}{\partial z} + \mu\left(\frac{\partial^2 w}{\partial r^2} + \frac{1}{r}\frac{\partial w}{\partial r}\right) - \sigma B_0^2 w - \frac{\mu}{K} w, \quad (1)$$

Where ρ is the fluid density, μ is the dynamic viscosity, σ is the electrical conductivity, B_0 is the magnetic-field strength, K is the permeability of the porous medium, and p is the pressure. Let the imposed pressure gradient be constant and defined by $-\frac{\partial p}{\partial z} = G, G > 0$. Then the dimensional governing equation becomes:

$$\rho \frac{\partial w}{\partial t} = G + \mu\left(\frac{\partial^2 w}{\partial r^2} + \frac{1}{r}\frac{\partial w}{\partial r}\right) - \sigma B_0^2 w - \frac{\mu}{K} w. \quad (2)$$

The fluid is initially at rest:

$$w(r, 0) = 0, R_1 \leq r \leq R_2. \quad (3)$$

Since the cylinders are stationary, the no-slip boundary conditions are:

$$w(R_1, t) = 0, w(R_2, t) = 0, t > 0, \quad (4)$$

The dimensional wall shear stresses are:

$$\tau_{R_1} = \mu \frac{\partial w}{\partial r}\bigg|_{r=R_1}, \quad (5)$$

and

$$\tau_{R_2} = \mu \frac{\partial w}{\partial r}\bigg|_{r=R_2}. \quad (6)$$

2.2 Dimensionless governing equations

Introduce the dimensionless variables:

$$\eta = \frac{r}{R_2}, \lambda = \frac{R_1}{R_2}, T = \frac{\nu t}{R_2^2}, u(\eta, T) = \frac{\mu w(r,t)}{G R_2^2}, \nu = \frac{\mu}{\rho}, M^2 = \frac{\sigma B_0^2 R_2^2}{\mu}, Da = \frac{K}{R_2^2}. \tag{7}$$

ν is the kinematic viscosity, and λ is the radius ratio, M is the Hartmann number. The annular domain becomes, $\lambda \leq \eta \leq 1$.

Using these definitions, the non-dimensional governing equation becomes:

$$\frac{\partial u}{\partial T} = \frac{\partial^2 u}{\partial \eta^2} + \frac{1}{\eta}\frac{\partial u}{\partial \eta} - \alpha^2 u + 1. \tag{8}$$

where $\alpha^2 = M^2 + \frac{1}{Da}$.

The dimensionless initial condition is

$$u(\eta, 0) = 0, \lambda \leq \eta \leq 1, \tag{9}$$

and the dimensionless boundary conditions are

$$u(\lambda, T) = 0, u(1, T) = 0, T > 0. \tag{10}$$

The parameter $\alpha^2 = M^2 + \frac{1}{Da}$ shows that magnetic resistance and porous resistance enter the momentum equation additively. Hence, both mechanisms act as linear damping forces against the pressure-driven axial motion.

3 Solution

The dimensionless problem is solved using the Laplace transform in time. Let the Laplace transform of function as defined in the work of [24] be

$$\bar{u}(\eta, s) = \mathcal{L}\{u(\eta, T)\} = \int_0^\infty e^{-sT}\, u(\eta, T)\, dT. \tag{11}$$

Applying the Laplace transform to equations (8) and (9) and simplifications, we obtain:

$$\frac{d^2 \bar{u}}{d\eta^2} + \frac{1}{\eta}\frac{d\bar{u}}{d\eta} - \beta^2 \bar{u} = -\frac{1}{s}. \tag{12}$$

where $\beta^2 = s + \alpha^2$.

The associated homogeneous equation is a modified Bessel equation of order zero. Therefore, the transformed solution has the form:

$$\bar{u}(\eta, s) = AI_0(\beta\eta) + BK_0(\beta\eta) + \frac{1}{s\beta^2}, \tag{13}$$

where I_0 and K_0 are modified Bessel functions of the first and second kinds of order zero.

The transformed boundary conditions are:

$$\bar{u}(\lambda, s) = 0, \bar{u}(1, s) = 0. \tag{14}$$

Hence, A and B, are obtained as:

$$A = \frac{K_0(\beta) - K_0(\beta\lambda)}{s\beta^2[I_0(\beta)K_0(\beta\lambda) - I_0(\beta\lambda)K_0(\beta)]},$$

and

$$B = \frac{I_0(\beta\lambda) - I_0(\beta)}{s\beta^2[I_0(\beta)K_0(\beta\lambda) - I_0(\beta\lambda)K_0(\beta)]}.$$

3.1 Velocity profile

The velocity profile is obtained in two forms: the transient velocity profile in the Laplace domain and the steady-state velocity profile in closed form.

3.1.1 Unsteady velocity profile

Substitution of the constants A and B into the transformed velocity field (13) gives:

$$\bar{u}(\eta, s) = \frac{1}{s\beta^2}\left[1 + \frac{\{K_0(\beta) - K_0(\beta\lambda)\}I_0(\beta\eta) + \{I_0(\beta\lambda) - I_0(\beta)\}K_0(\beta\eta)}{I_0(\beta)K_0(\beta\lambda) - I_0(\beta\lambda)K_0(\beta)}\right] \tag{15}$$

Where $\beta = \sqrt{s + \alpha^2}$. The corresponding time-domain velocity is formally

$$u(\eta, T) = \mathcal{L}^{-1}\{\bar{u}(\eta, s)\}. \tag{16}$$

Since the transformed solution contains modified Bessel functions with complex Laplace parameter s, direct analytical inversion is generally not convenient. Therefore, the Riemann-sum approximation method is employed to recover the transient solution numerically.

3.1.2 Steady velocity profile

At steady state, $\frac{\partial u}{\partial T} = 0$. Therefore, equation (8) is reduced to:

$$\frac{d^2u_s}{d\eta^2} + \frac{1}{\eta}\frac{du_s}{d\eta} - \alpha^2 u_s = -1. \tag{17}$$

The steady solution is:

$$u_s(\eta) = CI_0(\alpha\eta) + DK_0(\alpha\eta) + \frac{1}{\alpha^2}. \tag{18}$$

Using

$$u_s(\lambda) = 0, u_s(1) = 0, \tag{19}$$

we obtain:

$$C = \frac{K_0(\alpha) - K_0(\alpha\lambda)}{\alpha^2[I_0(\alpha)K_0(\alpha\lambda) - I_0(\alpha\lambda)K_0(\alpha)]},$$

and

$$\mathrm{D} = \frac{I_0(\alpha\lambda) - I_0(\alpha)}{\alpha^2[I_0(\alpha)K_0(\alpha\lambda) - I_0(\alpha\lambda)K_0(\alpha)]}.$$

respectively.

Thus, the steady velocity profile is:

$$u_s(\eta) = \frac{1}{\alpha^2}\left[1 + \frac{\{K_0(\alpha) - K_0(\alpha\lambda)\}I_0(\alpha\eta) + \{I_0(\alpha\lambda) - I_0(\alpha)\}K_0(\alpha\eta)}{I_0(\alpha)K_0(\alpha\lambda) - I_0(\alpha\lambda)K_0(\alpha)}\right]. \tag{20}$$

This expression represents the limiting velocity distribution approached by the transient solution as $T \to \infty$.

3.2 Skin friction

The dimensionless skin friction is proportional to the radial derivative of the dimensionless velocity. Define by: $C_f(\eta, T) = \frac{\partial u}{\partial \eta}$.

The inner-wall and outer-wall skin frictions are respectively $C_{f,\lambda}(T) = \left.\frac{\partial u}{\partial \eta}\right|_{\eta=\lambda}$, and $C_{f,1}(T) = \left.\frac{\partial u}{\partial \eta}\right|_{\eta=1}$. Because the velocity satisfies the no-slip condition at both walls, these quantities measure the shear response of the annular boundaries.

3.2.1 Unsteady skin friction

In the Laplace domain,

$$\bar{C}_{f,\lambda}(s) = \left[\frac{\{K_0(\beta) - K_0(\beta\lambda)\}I_1(\beta\lambda) - \{I_0(\beta\lambda) - I_0(\beta)\}K_1(\beta\lambda)}{s\beta[I_0(\beta)K_0(\beta\lambda) - I_0(\beta\lambda)K_0(\beta)]}\right]. \tag{21}$$

and

$$\bar{C}_{f,1}(s) = \left[\frac{\{K_0(\beta) - K_0(\beta\lambda)\}I_1(\beta) - \{I_0(\beta\lambda) - I_0(\beta)\}K_1(\beta)}{s\beta[I_0(\beta)K_0(\beta\lambda) - I_0(\beta\lambda)K_0(\beta)]}\right]. \tag{22}$$

The time-domain unsteady skin frictions are obtained through inverse Laplace transformation:

$$C_{f,\lambda}(T) = \mathcal{L}^{-1}\{\bar{C}_{f,\lambda}(s)\}, \tag{23}$$

$$C_{f,1}(T) = \mathcal{L}^{-1}\{\bar{C}_{f,1}(s)\}. \tag{24}$$

3.2.2 Steady skin friction

The steady velocity is:

$$u_s(\eta) = C_1 I_0(\alpha\eta) + C_2 K_0(\alpha\eta) + \frac{1}{\alpha^2}. \tag{25}$$

Therefore, the steady skin friction at the inner and outer cylinders is:

$$C_{f,\lambda}^{(s)} = \frac{[K_0(\alpha)-K_0(\alpha\lambda)]I_1(\alpha\lambda)-[I_0(\alpha\lambda)-I_0(\alpha)]K_1(\alpha\lambda)}{\alpha[I_0(\alpha)K_0(\alpha\lambda)-I_0(\alpha\lambda)K_0(\alpha)]}, \tag{26}$$

$$C_{f,1}^{(s)} = \frac{[K_0(\alpha)-K_0(\alpha\lambda)]I_1(\alpha)-[I_0(\alpha\lambda)-I_0(\alpha)]K_1(\alpha)}{\alpha[I_0(\alpha)K_0(\alpha\lambda)-I_0(\alpha\lambda)K_0(\alpha)]}. \tag{27}$$

These steady expressions provide reference values for assessing the large-time behaviour of the transient skin-friction solution.

3.3 Riemann-sum Approximation of Laplace Inversion

The Riemann-sum approximation is used to invert the Laplace-domain velocity and skin-friction functions numerically. For a Laplace-domain function $\bar{F}(s)$, the inverse transform is approximated by:

$$F(T,\eta) = \frac{e^{\varepsilon T}}{T}\left[\frac{1}{2}\bar{F}(\varepsilon,\eta) + \mathrm{Re}\sum_{k=1}^{N}\bar{F}\left(\varepsilon + \frac{ik\pi}{T},\eta\right)(-1)^k\right], \tag{28}$$

where $i = \sqrt{-1}, N$ is the number of terms retained in the finite summation, and ε is a positive convergence parameter. For the velocity field, inner-wall skin friction, and outer-wall skin friction, representing $F(T)$ and we have

$$u(T,\eta) = \frac{e^{\varepsilon T}}{T}\left[\frac{1}{2}\bar{u}(\varepsilon,\eta) + \mathrm{Re}\sum_{k=1}^{N}\bar{u}\left(\varepsilon + \frac{ik\pi}{T},\eta\right)(-1)^k\right], \tag{29}$$

$$C_{f,\lambda}(T) = \frac{e^{\varepsilon T}}{T}\left[\frac{1}{2}\bar{C}_{f,\lambda}(\varepsilon) + \mathrm{Re}\sum_{k=1}^{N}\bar{C}_{f,\lambda}\left(\varepsilon + \frac{ik\pi}{T}\right)(-1)^k\right], \tag{30}$$

$$C_{f,1}(T) = \frac{e^{\varepsilon T}}{T}\left[\frac{1}{2}\bar{C}_{f,1}(\varepsilon) + \mathrm{Re}\sum_{k=1}^{N}\bar{C}_{f,1}\left(\varepsilon + \frac{ik\pi}{T}\right)(-1)^k\right]. \tag{31}$$

In numerical implementation, sufficiently large N is selected to ensure convergence. A common practical criterion is to choose the convergence parameter such that $\varepsilon T \approx 4.7$, although the optimal choice may depend on the time level and parameter range.

4 Results and Discussion

The semi-analytical results describe the start-up development of an electrically conducting Newtonian fluid driven by a constant axial pressure gradient through a porous annular region. The velocity field and the wall shear stress are controlled by the dimensionless time T, Hartmann number M, Darcy number Da, and radius ratio λ. The combined resistance parameter $\alpha^2 = M^2 + \frac{1}{Da}$ shows that magnetic damping and porous drag enter the momentum balance as additive linear resistance mechanisms. Therefore, the flow response depends not only on the individual values of M and Da, but also on their combined contribution to the effective hydromagnetic-porous damping. This type of transient annular-flow response is consistent with previous semi-analytical studies of unsteady annular and Dean-type flows, where the Laplace-transform/Riemann-sum approach was shown to capture the transition from initial motion to steady state [1], [25].

4.1 Transient development of the axial velocity

Figure 2 presents the effect of dimensionless time T on the velocity profile for $M = 1.0$ and $Da = 0.1$. At the initial stage, the velocity is small because the fluid starts from rest and the pressure-gradient impulse has not yet diffused fully across the annular gap. As T increases, the velocity increases throughout the annulus and gradually approaches a limiting steady profile. The no-slip condition is satisfied at both cylindrical walls, while the maximum velocity occurs within the annular gap rather than at the boundaries.

The profile is not exactly symmetric about the middle of the gap because the governing diffusion operator contains the cylindrical curvature term $(1/\eta)(\partial u/ \partial\eta)$. This curvature effect distinguishes annular flow from plane Poiseuille flow and causes the radial distribution of momentum to depend on the local radius. The observed transient-to-steady evolution in Figure 2 confirms that the unsteady solution asymptotically recovers the steady-state solution as $T \to \infty$, which is a necessary consistency condition for the Laplace-domain formulation.

The numerical results in Table 1 support this behaviour. For example, at $Da = 0.1$, $M = 0.5$, and $\eta = 0.6$, the RSA velocity increases from 0.0480 at $T = 0.2$ to 0.0484 at $T = 0.4$, matching the reported steady-state value of 0.0484. Similarly, for $Da = 1.0$, $M = 0.5$, and $\eta = 0.6$, the RSA velocity increases from 0.0737 at $T = 0.2$ to 0.0769 at $T = 0.4$, approaching the steady-state value of 0.0770. The agreement between the Riemann-sum approximation and the exact/benchmark solution improves as time increases, showing that the inversion procedure accurately captures the long-time flow development.

4.2 Influence of Hartmann number on velocity

Figure 3 shows the influence of the Hartmann number M on the velocity profile for fixed $T = 0.02$ and $Da = 0.1$. The velocity decreases as M increases. This is physically expected because the magnetic term $-M^2u$ represents Lorentz-force damping. When an electrically conducting fluid moves in the presence of an imposed magnetic field, induced currents interact with the magnetic field, generating a body force that opposes the motion. Hence, increasing M strengthens electromagnetic braking and suppresses the axial velocity.

The same trend is observed in Table 1. At $T = 0.2$, $Da = 0.1$, and $\eta = 0.6$, increasing M from 0.5 to 1.0 reduces the RSA velocity from 0.0480 to 0.0466. At $Da = 1.0$, the corresponding reduction is from 0.0737 to 0.0707. The reduction is also present at steady state, where the velocity at $\eta = 0.6$ decreases from 0.0484 to 0.0469 for $Da = 0.1$, and from 0.0770 to 0.0735 for $Da = 1.0$. This confirms that M acts as a flow-suppressing parameter in both the transient and fully developed regimes.

This magnetic damping behaviour agrees with established MHD internal-flow results, where the Hartmann number controls the strength of Lorentz-force resistance and reduces the momentum of conducting fluids in channels and annuli [20], [23]. In practical terms, the magnetic field provides an active control mechanism for reducing the flow rate without changing the geometry or the pressure gradient.

4.3 Influence of Darcy number on velocity

Figure 4 illustrates the effect of the Darcy number Da on the velocity distribution for fixed $T = 0.02$and $M = 1.0$. The velocity increases with increasing Da. This trend follows directly from the porous resistance term $-u/Da$. A small Darcy number corresponds to low permeability and strong resistance from the porous matrix, while a larger Darcy number indicates a more permeable medium that allows the fluid to move more freely.

The numerical values in Table 1 confirm this permeability effect. At $T = 0.2$, $M = 0.5$, and $\eta = 0.6$, the RSA velocity is 0.0480 for $Da = 0.1$, but increases to 0.0737 for $Da = 1.0$. At steady state under the same M and η, the velocity increases from 0.0484 to 0.0770 as Da increases from 0.1 to 1.0. Similar behaviour is observed for $M = 1.0$, where the steady velocity at $\eta = 0.6$ increases from 0.0469 to 0.0735 when Da increases from 0.1 to 1.0.

This result is consistent with classical porous-media theory, where permeability determines the ease with which fluid penetrates the porous skeleton [11]. It also agrees with previous studies on pressure-driven flow in porous annular and composite-channel systems, in which porous resistance was shown to reduce the velocity magnitude and delay the development of the flow field [13], [14]. In the present model, increasing Da reduces $1/Da$, thereby reducing α^2 and weakening the total resistance to the pressure-driven motion.

4.4 Numerical validation of the velocity solution

Table 1 provides a quantitative comparison between the RSA results and the ES values for different T, M, Da, and η. The table demonstrates three important features of the solution.

First, the maximum velocity occurs inside the annular gap. For instance, at $T = 0.2$, $M = 0.5$, and $Da = 0.1$, the RSA velocity increases from 0.0422 at $\eta = 0.4$ to 0.0480 at $\eta = 0.6$, and then decreases to 0.0344 at $\eta = 0.8$. This behaviour reflects the no-slip condition at the walls and the pressure-driven acceleration within the annulus.

Second, the transient velocity approaches the steady velocity as time increases. The RSA and ES values are already close at $T = 0.2$, become nearly identical at $T = 0.4$, and coincide to the reported decimal places at steady state. This agreement validates the Riemann-sum inversion used to recover the transient solution from the Laplace domain.

Third, the table confirms the opposite roles of M and Da. Increasing M decreases the velocity because of stronger Lorentz-force damping, while increasing Da increases the velocity because of weaker porous-medium resistance. These numerical trends are fully consistent with the governing resistance parameter $\alpha^2 = M^2 + 1/Da$.

4.5 Skin-friction response with time

Figure 5 shows the effect of dimensionless time on the skin friction at the inner cylinder $\eta = \lambda$ and the outer cylinder $\eta = 1$ for $M = 1.0$ and $Da = 0.1$. Since the skin friction is defined by the radial velocity gradient, $C_f = \frac{\partial u}{\partial \eta}$, it measures the shear transmitted from the developing fluid motion to the cylindrical walls.

At early times, the wall shear changes rapidly because the fluid accelerates from rest and steep near-wall gradients are generated by the no-slip boundaries. As time increases, the rate of variation decreases, and the skin-friction curves approach their steady-state limits. The opposite signs of the wall gradients are physically meaningful: the velocity rises from zero at the inner wall, giving a positive inner-wall gradient, and decreases to zero at the outer wall, giving a negative outer-wall gradient.

The values in Table 2 support this transient convergence. For $Da = 0.1$, $M = 0.5$, and $\lambda = 0.4$, the inner-wall RSA skin friction is 0.2822 at $T = 0.2$, 0.2824at $T = 0.4$, and 0.2822 at steady state. The small difference between the transient and steady values shows that the wall-shear response approaches its asymptotic limit rapidly for this parameter set. Similar convergence is obtained at the outer cylinder, where the magnitude of the wall shear also tends toward its steady value as T increases.

4.6 Effect of Hartmann number on skin friction

Figure 6 displays the effect of the Hartmann number on the skin friction at $\eta = \lambda$ and $\eta = 1$ for fixed $T = 0.02$ and $Da = 0.1$. Increasing M modifies the wall shear stress because magnetic damping reduces the axial momentum and changes the near-wall velocity gradient. The wall shear therefore depends not only on the reduction in velocity magnitude but also on how the magnetic field reshapes the velocity profile near the cylindrical surfaces.

Table 2 confirms this trend. At $Da = 0.1$, $T = 0.2$, and $\lambda = 0.4$, increasing M from 0.5 to 1.0 reduces the reported inner-wall skin friction from 0.2822 to 0.2775. At steady state for the same Da and λ, the inner-wall value decreases from 0.2822 to 0.2775, while the outer-wall shear magnitude also decreases slightly. This demonstrates that the Hartmann number suppresses both the core velocity and the wall-shear response under the present parameter range.

This behaviour agrees with the classical interpretation of MHD flow control: an imposed magnetic field damps the motion of a conducting fluid and reduces momentum transport across the flow domain. The result is important in engineering applications where magnetic fields are used to regulate liquid-metal or electrolyte flows in confined geometries.

4.7 Effect of Darcy number on skin friction

Figure 7 shows the effect of Darcy number on the skin friction at the inner and outer cylinders for fixed $T = 0.02$ and $M = 1.0$. Increasing Da reduces the resistance of the porous matrix, thereby increasing the axial velocity and strengthening the velocity gradients near the walls. Consequently, the magnitude of the wall shear generally increases as the medium becomes more permeable.

This trend is reflected in Table 2. At steady state, $M = 0.5$, and $\lambda = 0.4$, increasing Da from 0.1 to 1.0 increases the inner-wall shear from approximately 0.2822 to 0.3584, while the magnitude of the outer-wall shear increases from approximately 0.2119 to 0.2614. For $M = 1.0$, the same permeability increase raises the inner-wall shear from approximately 0.2775 to 0.3502, while the magnitude of the outer-wall shear increases from approximately 0.2088 to

0.2561. Thus, although a larger Darcy number enhances the flow, it also increases the shear transmitted to the walls.

This result is mechanically important. In porous annular systems, increasing permeability may improve throughput but also increase wall shear and associated surface stresses. Therefore, Da must be selected carefully in applications involving filtration, porous heat exchangers, oil-well annuli, and other systems where both flow rate and wall loading are relevant.

4.8 Effect of radius ratio on skin friction

Table 2 also shows the influence of the radius ratio λ on the wall shear stress. For a fixed T, M, and Da, the magnitude of the skin friction generally decreases as λ increases from 0.4 to 0.8. For example, at $T = 0.2$, $M = 0.5$, and $Da = 0.1$, the inner-wall RSA skin friction decreases from 0.2822 at $\lambda = 0.4$ to 0.1008 at $\lambda = 0.8$. This reduction indicates that the annular geometry strongly affects the distribution of radial velocity gradients.

The radius ratio controls the gap width and the degree of wall confinement. As λ changes, the annular area, curvature effects, and momentum-diffusion length scale are all modified. Therefore, the skin-friction response cannot be interpreted only in terms of M and Da; the geometry of the annulus also plays a significant role. Similar geometric sensitivity has been reported in annular and Taylor-Couette-type flow studies, where radius ratio affects velocity structure, stability, and wall shear [2], [4].

4.9 Reliability of the semi-analytical solution

The agreement between RSA and large-time RSA values in Tables 1 and 2 confirms the reliability of the semi-analytical procedure. The Laplace transform reduces the time-dependent governing equation to a radial boundary-value problem involving modified Bessel functions, while the Riemann-sum approximation recovers the transient solution without direct time marching. The convergence of RSA values to the corresponding steady-state values further verifies that the numerical inversion is consistent with the independently derived steady solution at large time.

For the velocity field, Table 1 shows that RSA and large time RSA values become nearly identical by $T = 0.4$ and coincide at steady state. For the skin friction, Table 2 shows the same pattern: the transient wall-shear values approach the steady wall-shear values as time increases. This dual validation, through both velocity and wall shear stress, strengthens confidence in the analytical formulation and numerical inversion technique.

4.10 Physical and engineering implications

The results demonstrate that transient MHD flow in a porous annulus is governed by a balance among pressure forcing, viscous diffusion, Lorentz-force damping, Darcy resistance, and wall confinement. Increasing M suppresses the velocity and reduces wall shear by strengthening electromagnetic damping. Increasing Da enhances velocity by reducing porous drag, but it also increases wall shear magnitude because stronger flow produces larger near-wall gradients. The radius ratio λ provides an additional geometric control parameter by modifying the annular gap width and the curvature-dependent momentum distribution.

These results are relevant to electromagnetic flow-control systems, liquid-metal cooling channels, porous filtration units, petroleum-production annuli, geothermal transport systems, and industrial devices involving electrically conducting fluids in porous cylindrical passages. The study shows that the flow rate can be controlled actively through the magnetic field and passively through the permeability of the porous matrix. Therefore, the combined parameter $\alpha^2 = M^2 + 1/Da$ provides a useful design measure for predicting and regulating hydromagnetic transport in porous annular systems.

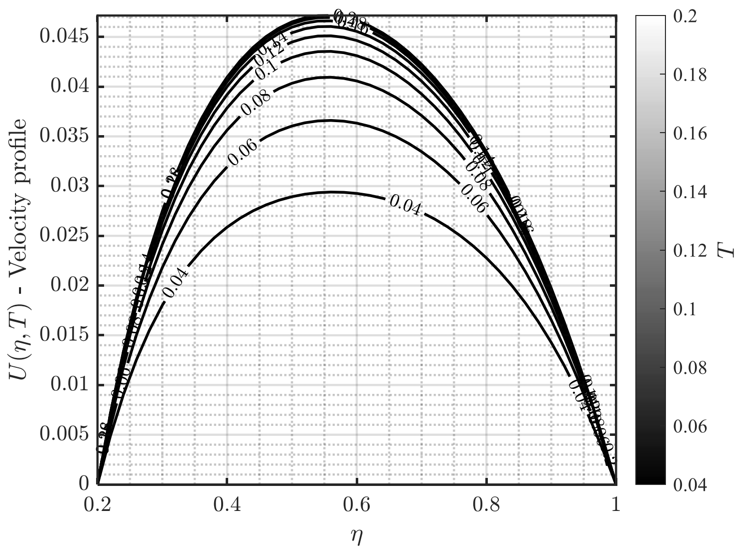

Figure 2: Effect of dimensionless time (T) on the velocity profile for $M = 1.0$, $Da = 0.1$.

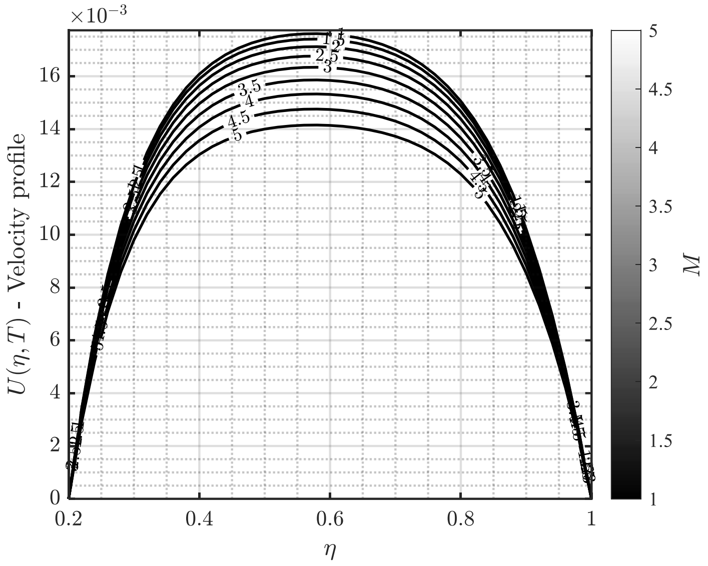

Figure 3: Effect of Hartmann number (M) on the velocity profile for fixed $T = 0.02$, $Da = 0.1$.

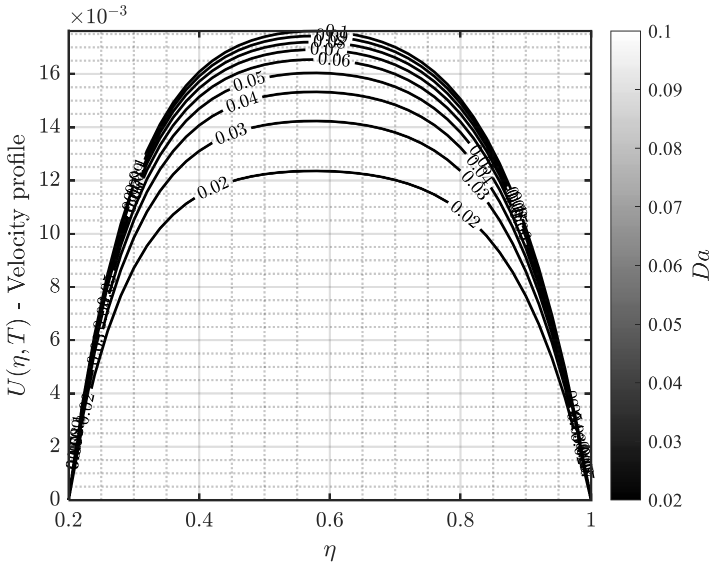

Figure 4: Variation of Darcy number (Da) on the velocity profile for fixed $T = 0.02$, $M = 1.0$.

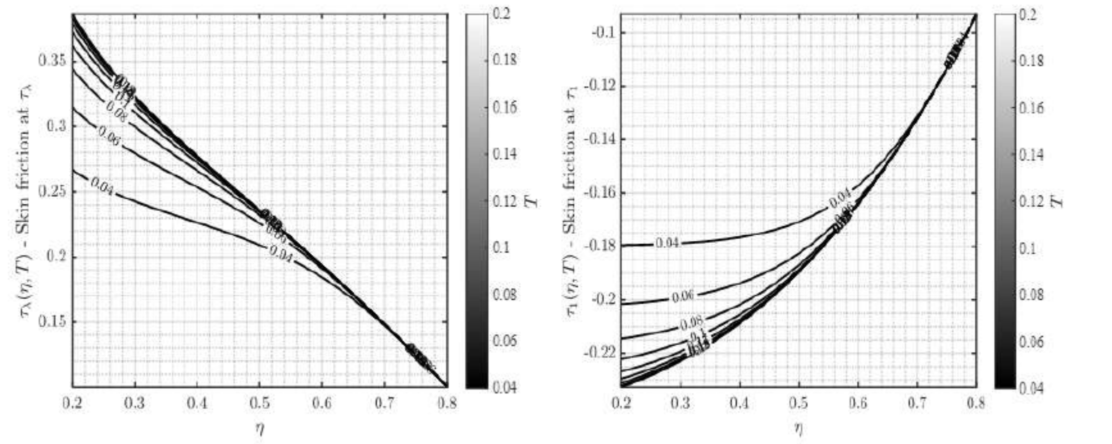

Figure 5a

Figure 5b

Figure 5: Effect of dimensionless time (T) on (a) the skin friction at $\eta = \lambda$ and (b) the skin friction at $\eta = 1$ for $M = 1.0$, $Da = 0.1$.

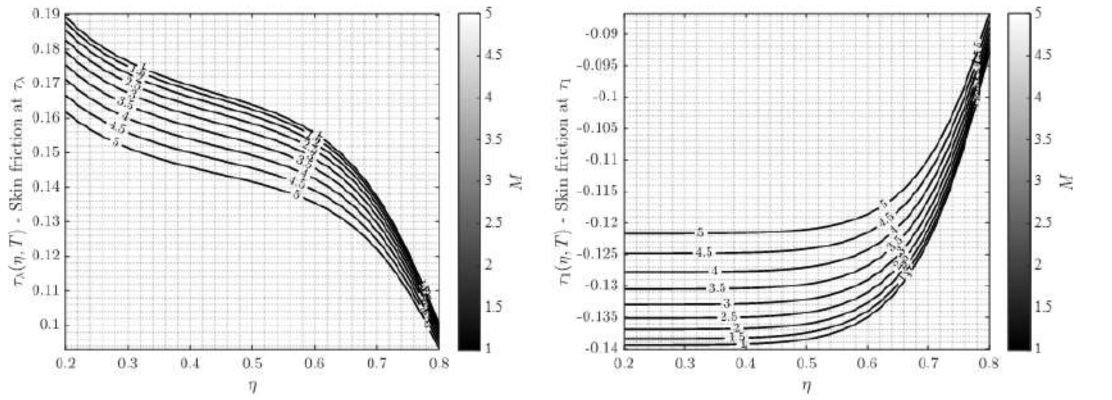

Figure 6a

Figure 6b

Figure 6: Effect of Hartmann number (M) on (a) the skin friction at $\eta = \lambda$ and (b) the skin friction at $\eta = 1$ for fixed $T = 0.02$, $Da = 0.1$.

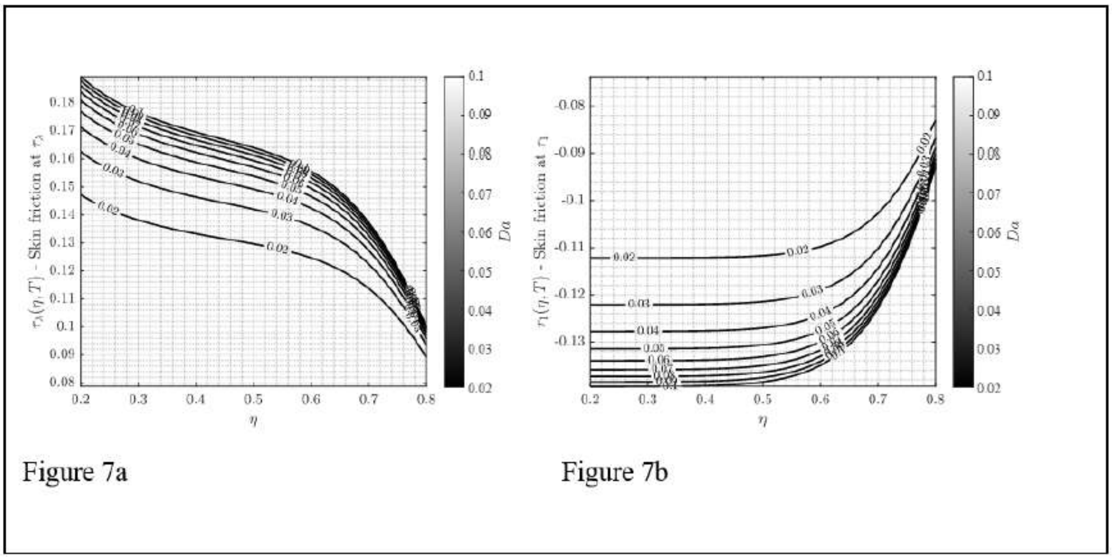

Figure 7: Variation of Darcy number (Da) on (a) the skin friction at $\eta = \lambda$ and (b) the skin friction at $\eta = 1$ for fixed $T = 0.02$, $M = 1.0$.

Table 1: Numerical values of axial velocity profile for different values of T, M, and Da.

Velocity profile						
			$Da = 0.1$		$Da = 1.0$	
T	M	η	RSA	Steady-state	RSA	Steady-state
0.2	0.5	0.4	0.0422	0.0425	0.0645	0.0674
		0.6	0.0480	0.0484	0.0737	0.0770
		0.8	0.0344	0.0346	0.0505	0.0525
	1.0	0.4	0.0410	0.0412	0.0619	0.0643
		0.6	0.0466	0.0469	0.0707	0.0735
		0.8	0.0335	0.0336	0.0486	0.0503
0.4	0.5	0.4	0.0425	0.0425	0.0673	0.0674
		0.6	0.0484	0.0484	0.0769	0.0770
		0.8	0.0346	0.0346	0.0524	0.0525
	1.0	0.4	0.0412	0.0412	0.0642	0.0643
		0.6	0.0469	0.0469	0.0734	0.0735
		0.8	0.0336	0.0336	0.0502	0.0503
10^4	0.5	0.4	0.0425	0.0425	0.0674	0.0674
		0.6	0.0484	0.0484	0.0770	0.0770
		0.8	0.0346	0.0346	0.0525	0.0525
	1.0	0.4	0.0412	0.0412	0.0643	0.0643
		0.6	0.0469	0.0469	0.0735	0.0735
		0.8	0.0336	0.0336	0.0503	0.0503

Table 2: Numerical values of the skin friction at $\eta = \lambda$ and $\eta = 1$ for different values of T, M, and Da.

			Skin friction at $\eta = \lambda$				Skin friction at $\eta = 1$			
			$Da = 0.1$		$Da = 1.0$		$Da = 0.1$		$Da = 1.0$	
T	M	λ	RSA	Steady State	RSA	Steady State	RSA	Steady State	RSA	Steady State
0.2	0.5	0.4	0.2822	0.2822	-0.2119	-0.2119	0.3574	0.3584	-0.2608	-0.2614
		0.6	0.1950	0.1949	-0.1655	-0.1654	0.2184	0.2182	-0.1839	-0.1838
		0.8	0.1008	0.1007	-0.0936	-0.0935	0.1038	0.1037	-0.0964	-0.0963
	1.0	0.4	0.2775	0.2775	-0.2088	-0.2088	0.3494	0.3502	-0.2556	-0.2561
		0.6	0.1933	0.1932	-0.1642	-0.1640	0.2162	0.2160	-0.1822	-0.1821
		0.8	0.1005	0.1004	-0.0934	-0.0933	0.1036	0.1035	-0.0961	-0.0960
0.4	0.5	0.4	0.2824	0.2822	-0.2120	-0.2119	0.3585	0.3584	-0.2615	-0.2614
		0.6	0.1950	0.1949	-0.1655	-0.1654	0.2184	0.2182	-0.1840	-0.1838
		0.8	0.1008	0.1007	-0.0937	-0.0935	0.1039	0.1037	-0.0964	-0.0963
	1.0	0.4	0.2777	0.2775	-0.2089	-0.2088	0.3504	0.3502	-0.2563	-0.2561
		0.6	0.1933	0.1932	-0.1642	-0.1640	0.2162	0.2160	-0.1822	-0.1821
		0.8	0.1006	0.1004	-0.0935	-0.0933	0.1036	0.1035	-0.0962	-0.0960
10^4	0.5	0.4	0.2822	0.2822	-0.2119	-0.2119	0.3584	0.3584	-0.2614	-0.2614
		0.6	0.1949	0.1949	-0.1654	-0.1654	0.2182	0.2182	-0.1838	-0.1838
		0.8	0.1007	0.1007	-0.0935	-0.0935	0.1037	0.1037	-0.0963	-0.0963
	1.0	0.4	0.2775	0.2775	-0.2088	-0.2088	0.3502	0.3502	-0.2561	-0.2561
		0.6	0.1932	0.1932	-0.1640	-0.1640	0.2160	0.2160	-0.1821	-0.1821
		0.8	0.1004	0.1004	-0.0933	-0.0933	0.1035	0.1035	-0.0960	-0.0960

5 Conclusion

A semi-analytical formulation has been presented for transient magnetohydrodynamic axial flow of an incompressible, viscous, electrically conducting fluid through a porous annulus bounded by two stationary concentric cylinders. The flow is driven by a constant axial pressure gradient and subjected to a uniform transverse magnetic field. Darcy resistance was included to model porous-medium drag, while the Lorentz-force term was used to represent magnetic damping.

After non-dimensionalization, the governing equation was reduced to a linear transient problem controlled mainly by the Hartmann number M, Darcy number Da, and radius ratio λ. The Laplace transform method was used to obtain the transformed velocity solution, and the Riemann-sum approximation was employed to recover the transient velocity and skin-friction profiles. Steady-state expressions were also obtained for comparison with the large-time behaviour of the transient solution. The main findings are as follows:

1. Increasing the Hartmann number suppresses the axial velocity because of stronger Lorentz-force damping.
2. Increasing the Darcy number enhances the axial velocity by reducing the resistance of the porous medium.
3. Magnetic and porous effects combine through the effective resistance parameter $\alpha^2 = M^2 + \frac{1}{Da}$.
4. The transient velocity develops from the initial rest condition and approaches the steady-state profile as time increases.
5. The skin friction at the annular walls approaches its steady-state value at large time.
6. The radius ratio affects the wall shear stress by modifying the annular gap and the radial distribution of velocity gradients.

The results provide a semi-analytical description of transient hydromagnetic flow in a porous annulus. The formulation may be useful as a reference solution for idealized studies of electrically conducting fluids in porous annular geometries.

References

[1] B. K. Jha and Y. J. Danjuma, "Transient Dean flow in a channel with suction/injection: A semi-analytical approach," *Proceedings of the Institution of Mechanical Engineers, Part E: Journal of Process Mechanical Engineering*, vol. 233, no. 5, pp. 1036–1044, 2019, doi: 10.1177/0954408919825718.

[2] B. K. Jha and J. D. Yahaya, "Transient Dean flow in an annulus: a semi-analytical approach," *Journal of Taibah University for Science*, vol. 13, no. 1, pp. 169–176, 2018, doi: 10.1080/16583655.2018.1549529.

[3] Y. J. Danjuma, *Transient Flow Formation inside an Annulus: A Semi-Analytical Approach*. DE, 2019. [Online]. Available:

https://www.morebooks.de/store/gb/book/transient-flow-formation-inside-an-annulus:-a-semi-analytical-approach/isbn/978-620-0-23920-4

[4] B. K. Jha and Y. J. Danjuma, “Transient generalized Taylor-Couette flow: a semi-analytical approach,” *Journal of Taibah University for Science*, vol. 14, no. 1, pp. 445–453, 2020, doi: 10.1080/16583655.2020.1745477.

[5] S. T. Wereley and R. M. Lueptow, “Velocity field for Taylor–Couette flow with an axial flow,” *Physics of Fluids*, vol. 11, no. 12, pp. 3637–3648, 1999.

[6] R. M. Lueptow, A. Docter, and K. Min, “Stability of axial flow in an annulus with a rotating inner cylinder,” *Physics of Fluids A*, vol. 4, no. 11, pp. 2446–2558, 1992.

[7] U. K. Sarkar and N. Biswas, “Exact and limiting solutions of fluid flow for axially oscillating cylindrical pipe and annulus,” *SN Appl. Sci.*, vol. 3, no. 3, p. 339, 2021.

[8] G. Ali, M Ahmad, F. Ali, & A. Khan. Couette flow of viscoelastic dusty fluid through a porous oscillating plate in a rotating frame along with heat transfer. *Heat Transfer, 53*(8), 4588–4607. 2024, https://doi.org/10.1002/htj.23127

[9] Y. Zhang, & C. Liu. Unsteady magnetohydrodynamic oblique stagnation point slip flow of Maxwell fluid over an oscillating–stretching cylinder with Cattaneo–Christov double diffusion model. *Numerical Heat Transfer, Part B: Fundamentals, 86*(9), 3018–3038. 2024 https://doi.org/10.1080/10407790.2024.2352854

[10] T. Hayat, S. Qayyum, M. Imtiaz, and A. Alsaedi (2016). Magnetohydrodynamic (MHD) flow of Jeffrey fluid over a stretching cylinder with slip conditions and heat transfer. *Journal of Molecular Liquids, 220*, 846–854. https://doi.org/10.1016/j.molliq.2016.04.083

[11] J. Bear, *Dynamics of fluids in porous media*. Courier Corporation, 2013.

[12] A. S. Berman, “Laminar Flow in an Annulus with Porous Walls,” *J. Appl. Phys.*, vol. 29, no. 1, pp. 71–75, 1958, doi: 10.1063/1.1722948.

[13] B. K. Jha and T. S. Yusuf, “Transient pressure driven flow in an annulus partially filled with porous material: Azimuthal pressure gradient,” *Mathematical Modelling of Engineering Problems*, vol. 5, no. 3, pp. 260–267, 2018, doi: 10.18280/mmep.050320.

[14] B. K. Jha and T. S. Yusuf, “Transient Taylor—Dean flow in a composite annulus partially filled with porous material,” *Thermophysics and Aeromechanics*, vol. 29, no. 2, pp. 267–280, 2022.

[15] B. K. Jha and J. O. Odengle, “Unsteady Couette flow in a composite channel partially filled with porous material: A semi - analytical approach,” *Transp. Porous Media*, vol. 107, no. 1, pp. 219–234, 2015.

[16] T. H. Masood, K. M. Ayub, and A. M. Siddiqui, "The unsteady Couette flow of a second grade fluid in a layer of porous medium," *Archives of Mechanics*, vol. 57, no. 5, pp. 405–416, 2005.

[17] A. A. Avramenko and A. V Kuznetsov, "Flow in a Curved Porous Channel with a Rectangular Cross Section," *J. Porous Media*, vol. 11, no. 3, pp. 241–246, 2008, doi: 10.1615/JPorMedia.v11.i3.20.

[18] S. Aberkane, M. Ihdene, M. Moderes, and A. Ghezal, "Axial magnetic field effect on Taylor-Couette flow," *Journal of applied fluid mechanics*, vol. 8, no. 2, pp. 255–264, 2014.

[19] P. Dash, K. L. Ojha, and G. C. Dash, "Unsteady Dean flow between concentric circular cylinders in the presence of a uniform axial magnetic field," *Numerical Heat Transfer, Part B: Fundamentals*, vol. 86, no. 10, pp. 3562–3575, 2025.

[20] O. D. Makinde and T. Chinyoka, "MHD transient flows and heat transfer of dusty fluid in a channel with variable physical properties and Navier slip condition," *Computers and Mathematics with Applications*, vol. 60, no. 3, pp. 660–669, 2010, doi: 10.1016/j.camwa.2010.05.014.

[21] T. Gul, M. Jan, Z. Shah, S. Islam, and M. A. Khan, "Unsteady Transient Couette and Poiseuille Flow Under The effect Of Magneto-hydrodynamics and Temperature," *J. Appl. Environ. Biol. Sci*, vol. 5, no. 7, pp. 339–353, 2015.

[22] A. Kumar and A. Singh, "Transient magnetohydrodynamic Couette flow with ramped velocity," *International Journal of Fluid Mechanics Research*, vol. 37, no. 5, 2010.

[23] J. P. Maurya, S. Lal Yadav, and A. K. Singh, "Analysis of magnetohydrodynamics transient flow in a horizontal annular duct," *Int. J. Dyn. Control*, vol. 4, 2020, doi: 10.1007/s40435-020-00611-4.

[24] B. K. Jha and Y. J. Danjuma, "Transient generalized Taylor–Couette flow of a dusty fluid: A semi-analytical approach," *Partial Differential Equations in Applied Mathematics*, vol. 5, p. 100400, 2022.

[25] B. K. Jha and Y. J. Danjuma, "Unsteady Dean flow formation in an annulus with partial slippage: A riemann-sum approximation approach," *Results in Engineering*, vol. 5, p. 100078, Mar. 2020, doi: 10.1016/j.rineng.2019.100078.